An ab Initio and Classical Molecular Dynamics Investigation of the Structural and Vibrational Properties of Talc and Pyrophyllite

James P. Larentzos, Jeffery A. Greathouse,* and Randall T. Cygan

Geochemistry Department, Sandia National Laboratories, Albuquerque, New Mexico 87185-0754

Received: April 16, 2007; In Final Form: June 1, 2007

The structural and vibrational properties of two uncharged 2:1 phyllosilicates, talc and pyrophyllite, are investigated via ab initio and classical molecular dynamics simulations. The quantum mechanical simulations are based on plane−wave pseudopotential density functional theory (DFT), which is shown to be sufficiently accurate in predicting the clay mineral structural and vibrational properties. The classical molecular dynamics (MD) simulations, using the CLAYFF force field, faithfully reproduce the crystal structures with relatively simple analytical functions that include primarily nonbonded interactions. The adsorption properties in these clay minerals are strongly dependent upon the disposition of the hydroxyl group in the octahedral sheet. With the assistance of molecular simulation, the relationship between the hydroxyl group vibrational modes and the molecular-scale structure is explored. The talc hydroxyl groups are oriented perpendicular to the *ab* plane, while the presence of the dioctahedral vacancies associated with pyrophyllite significantly alters the hydroxyl group structural and vibrational character. Overall, a detailed comparison between the ab initio and the classical MD structural and vibrational properties provides guidance for future refinements to the empirical force field.

Introduction

Phyllosilicates, including the clay minerals talc and pyrophyllite, are associated with numerous environmental, agricultural, and industrial processes. Because of the lack of well-crystallized materials and their fine-grained nature, experimental determinations of crystal structure and mineral behavior for most clay minerals are difficult to obtain.[1,2] Molecular simulations,[3] however, provide an opportunity to evaluate the detailed structure and dynamics for idealized models of these complex clay phases, usually as a supplement to the limited X-ray diffraction and vibrational spectroscopy data. Interlayer cations are absent because of the uncharged nature of the 2:1 layering for talc and pyrophyllite; the layers are held together by van der Waals forces. The disposition of hydroxyl groups within the octahedral sheet, especially in response to the dioctahedral vacancy associated with pyrophyllite, uniquely contribute to the adsorption properties of the clay minerals.

A number of theoretical studies have focused on highly accurate quantum mechanical calculations to simulate uncharged clay minerals such as pyrophyllite,[4−12] talc,[5,13] and kaolinite.[14−18] Because of their computational expense, these techniques tend to be limited to static energy calculations to examine the bulk structure and vibrational normal modes.[9,13,14,17] With the continuing increase in computational power, it is now possible to include thermal effects via ab initio molecular dynamics simulations. As an example, the vibrational power spectrum of kaolinite[7,12,18] has been previously obtained by Fourier transform of the velocity autocorrelation function. Although these quantum-based techniques are appealing, they are still restricted to small system sizes and time scales. Classical simulations are an attractive alternative but do require the development of accurate empirical models to describe the interactions.

Recently, classical simulations of clays have included flexibility within the clay framework.[19−21] With these force fields, the motion of clay atoms is governed primarily by intramolecular (angle bend, bond stretch) parameters. The associated simulations are therefore costly considering the large number of energy terms and also suffer from transferability issues. The advantage of a completely bonded force field is that the intramolecular parameters can be fine-tuned to the experimental vibrational frequencies. We employ a simpler nonbonded force field known as CLAYFF[22] that provides for flexibility without bonded terms. Framework atoms interact with each other through nonbonded terms (electrostatic, van der Waals), although an O−H bond stretch term is required to prevent layer H atoms from drifting. CLAYFF has been used successfully on a variety of layered minerals to investigate bulk properties (*d* spacing, etc.)[22−24] and interfacial properties such as ion and water adsorption.[25−27]

In this paper, both ab initio and classical molecular dynamics simulations of end-member dioctahedral (pyrophyllite) and trioctahedral (talc) smectites are performed. By starting with these neutral clays, the structural and vibrational properties are investigated without the influence of interlayer water or cations. The structures for each clay were previously determined from single-crystal X-ray diffraction studies. Talc is a 2:1 trioctahedral clay, with a structural composition of $Mg_3(OH)_2(Si_4O_{10})$ and space group symmetry $C\bar{1}$.[28] The unit cell includes a two-dimensional periodic layer consisting of an octahedrally coordinated magnesium oxide sheet sandwiched between two tetrahedrally coordinated silicate sheets (see Figure 1). Pyrophyllite is also a 2:1 layered clay with a structural composition of $Al(OH)(Si_2O_5)$ and space group symmetry $C\bar{1}$.[29] In contrast to talc, each layer contains dioctahedrally coordinated aluminum oxide sheets. As shown in Figure 1, the aluminum atoms form an ordered, hexagonal ring structure surrounding each vacancy. The presence of the vacancy has a significant effect on hydroxyl group orientation as well as the adsorption properties.

* Corresponding author. Phone: (505) 284-4895. Fax: (505) 844-7354. E-mail: jagreat@sandia.gov.

10.1021/jp072959f CCC: $37.00
Published on Web 08/09/2007

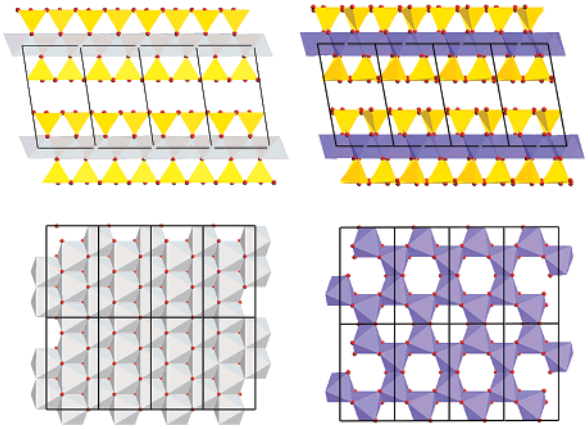

Figure 1. Two-layer polyhedral representation of talc (top, left) and pyrophyllite (top, right), where the metal oxide octahedral sheets (gray = Mg, blue = Al, yellow = Si, red = O, and white = H) are sandwiched between the silicate tetrahedral sheets. A top view comparison of the trioctahedral (bottom, left) and dioctahedral sheets (bottom, right) shows the vacancies present in pyrophyllite. The hydroxyl orientations have not been characterized experimentally and are not shown. See Figure 3 for hydroxyl group orientations.

TABLE 1: DFT Calculated Cell Lengths (Å), Cell Angles (degree), and Basal *d* Spacings for Talc and Pyrophyllite as Compared with Experiment[28,29]

	talc		pyrophyllite	
	DFT	expt	DFT	expt
a	5.259	5.290	5.119	5.160
b	9.129	9.173	8.911	8.966
c	9.250	9.460	9.065	9.347
α	90.12	90.46	90.77	91.18
β	99.32	98.68	100.96	100.46
γ	90.15	90.09	89.91	89.64
basal *d* spacing	9.128	9.351	8.90	9.190

Methods

DFT Optimizations. Periodic plane−wave DFT calculations were performed using the Vienna ab initio simulaton package (VASP).[30,31] The standard VASP suite of pseudopotentials was applied. Core electronic states were described using the accurate projector-augmented wave (PAW) approach[32,33] and the exchange-correlation functional was treated within the generalized gradient approximation (GGA) according to Perdew−Wang.[34] All DFT calculations were conducted with a 400 eV plane−wave cutoff energy. The clay unit cells were expanded into 2 × 1 × 2 supercells, providing two layers per supercell. Because of the sufficiently large simulation cells, the Brillouin-zone sampling was restricted to the Γ point.

To test the pseudopotentials, conjugate-gradient geometry optimizations were conducted on each clay supercell. The hydroxyl groups were initially oriented normal to the *ab* plane for both clays, since the locations have not been characterized through crystallographic studies. The optimizations were performed at constant pressure, where all lattice constants, cell angles, and atomic positions were free to relax without symmetry constraints. The optimized structure is compared with experiment in Table 1. Satisfactory agreement with the experimental lattice constants was observed. The lattice constants deviated from experiment by less than 1%, with exception to the *c* axis lengths. Underprediction of the *c* axis lengths caused the *d* spacings to be consistently 0.2−0.3 Å less than experiment. Previous DFT methods have overpredicted[4,8,12] and underpredicted[9,10] the *d* spacings of pyrophyllite by as much as 0.6 Å. Given that the pyrophyllite and talc layers interact predominantly through short-ranged dispersion forces, it is not surprising that the *c* axis dimension is not adequately captured through the DFT formalism. However, considering the previous studies, the pseudopotentials do provide an adequate description of the structural properties.

ab Initio Molecular Dynamics. Microcanonical ensemble (constant *NVE*) ab initio molecular dynamics (AIMD) simulations were conducted with full translational symmetry (*P*1 symmetry). To simplify postprocessing, the 2 × 1 × 2 triclinic supercells were converted into orthorhombic supercells. The orthorhombic supercell dimensions for pyrophyllite (160 atoms) were $a = 10.36$ Å, $b = 8.99$ Å, $c = 18.49$ Å and $a = 10.58$ Å, $b = 9.07$ Å, $c = 18.38$ Å for talc (168 atoms). The systems were equilibrated at 300 K for at least 20 ps and statistics were collected every 2 fs over 25 ps production runs. The velocity Verlet algorithm was used to update positions every time step, $\Delta t = 0.50$ fs. To reduce the energy drift to ∼1 K·ps^{-1}, the energy convergence tolerance for the electronic self-consistency loop at each Born Oppenheimer step was set to 10^{-7} eV.[35]

Classical Molecular Dynamics. For all classical simulations, orthorhombic unit cells were created from triclinic cells[22] and then expanded into an 8 × 4 × 3 supercell. Supercell dimensions for pyrophyllite (3840 atoms) were $a = 41.74$ Å, $b = 35.88$ Å, $c = 28.00$ Å, while for talc (4032 atoms) they were $a = 42.32$ Å, $b = 36.69$ Å, $c = 28.00$ Å.

Simulations were performed with the LAMMPS software as described previously.[25] Potential parameters (Table 2) were taken from the CLAYFF forcefield, which consists of nonbonded (electrostatic and van der Waals) terms for use with layered minerals.[22] For atoms *i* and *j* separated by a distance r_{ij}, the pairwise energy is given by the equation

$$E_{ij} = \frac{q_i q_j e^2}{4\pi\epsilon_0 r_{ij}} + D_0\left[\left(\frac{R_0}{r_{ij}}\right)^{12} - 2\left(\frac{R_0}{r_{ij}}\right)^{6}\right] \quad (1)$$

where q_i is the charge on atom *i*, *e* is the elementary charge on an electron, ϵ_0 is the permittivity of a vacuum, D_0 and R_0 are the 12−6 Lennard-Jones well depth and collision parameters, respectively. The only bonded parameter used was a harmonic bond stretching term for layer hydroxyl atoms (spring constant = 554.1349 kcal mol^{-1}, equilibrium bond length = 1.0 Å). Short-range interactions were evaluated every 0.5 fs with a cutoff of 10.0 Å. Arithmetic combining rules were used for off-diagonal van der Waals energy terms.[36] Long-range electrostatic interactions were evaluated every 1.0 fs using an efficient particle−particle particle-mesh Ewald summation algorithm.[37]

Following pre-equilibration runs of 0.05 and 0.1 ns in the *NVE* and *NVT* ensembles (N = number of atoms, V = volume, E = total potential energy, T = temperature), constant pressure (*NPT*) simulations of 1.25 ns in length were performed. The supercell was only allowed to expand or contract along the *c* axis, while the *a* and *b* axes (and cell angles) were fixed. Fluctuations of the *a* and *b* axes are expected to be small since a single clay layer is parallel to the *ab* plane. Thus, the *a* and *b* lengths are essentially controlled by intralayer (bonded) interactions. Indeed, fluctuations of the *a* and *b* axes lengths were quite small (≈ 0.05 Å) in previous MD simulations of pyrophyllite.[22] However, the *c* axis (and *d* spacing) length is dependent on layer−layer (nonbonded) interactions and is a

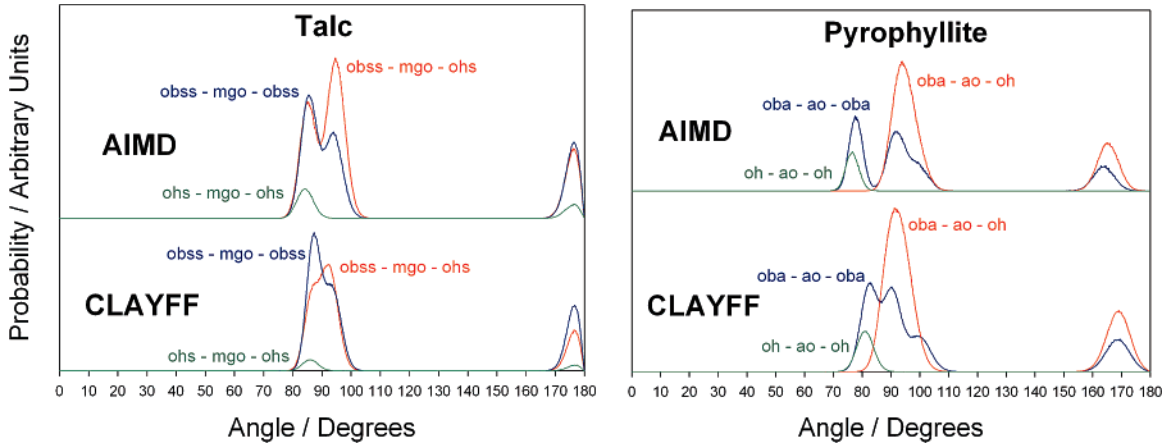

Figure 2. O−M−O [M = Al, Mg] angle distributions in talc (left) and pyrophyllite (right). The AIMD results are offset above the CLAYFF results. The oba atom label refers to the apical tetrahedral oxygen position but has the equivalent force field parameters as the ob CLAYFF atom type.

TABLE 2: Nonbonded Force Field Parameters for Pairwise Energy Terms between Atoms *i* and *j* Separated by a Distance *r*

mineral	species	atom type	q, e	D_0, kcal mol^{-1}	R_0, Å
pyrophyllite	octahedral aluminum	ao	1.5750	1.3298×10^{-6}	4.7943
	hydroxyl oxygen	oh	−0.9500	0.1554	3.5532
talc	octahedral magnesium	mgo	1.3600	9.0298×10^{-7}	5.9090
	apical oxygen	obss	−1.2996	0.1554	3.5532
	hydroxyl oxygen	ohs	−1.0808	0.1554	3.5532
both	Tetrahedral silicon	st	2.1000	1.8405×10^{-6}	3.7064
	bridging oxygen	ob	−1.0500	0.1554	3.5532
	hydroxyl hydrogen	ho	0.4250		

TABLE 3: CLAYFF and AIMD Bond Lengths (Å) Compared with Experiment[28,29]

	talc bond lengths				
	mgo-obss	mgo-oh	ob-st	obss-st	oh-ho
CLAYFF	2.09 ± 0.05	2.12 ± 0.06	1.59 ± 0.03	1.55 ± 0.03	1.03 ± 0.02
AIMD	2.07 ± 0.07	2.04 ± 0.06	1.62 ± 0.03	1.62 ± 0.03	0.96 ± 0.01
expt	2.06	2.03	1.62	1.62	
	pyrophyllite bond lengths				
	ao-oba	ao-oh	ob-st	oba-st	oh-ho
CLAYFF	1.98 ± 0.08	1.98 ± 0.08	1.56 ± 0.03	1.63 ± 0.04	1.03 ± 0.03
AIMD	1.92 ± 0.06	1.89 ± 0.05	1.62 ± 0.03	1.63 ± 0.03	0.97 ± 0.01
expt	1.90	1.92	1.61	1.63	

more critical validation of the force field parameters. The average lattice parameter (c) was calculated over the final 1.0 ns of simulation time. Although the calculated basal d spacings of 9.13 ± 0.01 Å (talc) and 9.31 Å ± 0.01 Å (pyrophyllite) are within 0.2 Å of experiment (Table 1), the experimental trend of $d_{talc} > d_{pyrophyllite}$ was not observed in the simulations. Equilibrium snapshots with the same c axis value were used for final *NVE* production runs. For structural information, the production run was 1.0 ns long with atomic positions stored every 1.0 ps.

Vibrational Analysis. Atomic velocity autocorrelation functions and their Fourier transformed power spectra were calculated using the TINKER software[38] with small modifications. For power spectra calculations, the atomic velocities were collected every 2 fs over a simulation time of 25 ps for the ab initio molecular dynamics simulations and 40 ps for the classical simulations. Sampling every 2 fs ensured that the vibrational modes up to 8000 cm^{-1} were captured. A windowing gap of 3000 frames (6.0 ps) was used to give a resolution of approximately 2.8 cm^{-1}. In some cases, the Fourier transform resulted in lobes around the peaks, which interfere with peak assignments. In these situations, the Welch and Parzen filtering methods were applied to resolve the vibrational peaks.[39] As an additional tool to assist with peak assignments, normal-mode analysis was conducted with the DMOL^3 and Discover software within Materials Studio 4.1.[40]

Results

To assess the ability of the CLAYFF forcefield and the VASP pseudopotentials to predict the clay structural properties, the bond and angle lengths are compared with experiment in Tables 3 and 4. Each atom is classified by the atom type definitions reported in Table 2, giving a total of 5 bond types and 10 angle types for each clay. Note that within the CLAYFF description of pyrophyllite, there is no distinction between apical (oba) and bridging (ob) siloxane oxygen parameters. However, for the bond and angle analysis, this distinction is made. All experimental bond and angle lengths were determined from the crystallographic structures.[28,29] The hydroxyl orientations have not been determined from diffraction experiments. Thus the bond lengths and angles involving the hydroxyl groups are not reported in the tables.

The average computed bond lengths for talc and pyrophyllite are all within 5% of experiment, as shown in Table 3. Even more encouraging, the CLAYFF forcefield and VASP pseudo-

TABLE 4: CLAYFF and AIMD Angles (degree) Compared with Experiment[28,29]

	talc angles									
	O−M−O			M−O−H	M−O−M		Si-O−M		O-Si-O	
	obss-mgo-obss	oh-mgo-obss	ohs-mgo-ohs	mgo-oh-ho	mgo-obss-mgo	mgo-oh-mgo	st-ob-st	st-obss-mgo	obss-st-ob	ob-st-ob
CLAYFF	87 ± 2	86 ± 2	86 ± 3	123 ± 9	93 ± 3	93 ± 3	147 ± 3	123 ± 3	106 ± 2	112 ± 3
	93 ± 3	92 ± 3	176 ± 2							
	175 ± 2	176 ± 2								
AIMD	85 ± 3	85 ± 3	84 ± 3	121 ± 8	94 ± 3	95 ± 3	137 ± 4	122 ± 3	109 ± 3	109 ± 4
	94 ± 3	95 ± 3	176 ± 3							
	176 ± 2	176 ± 2								
expt	83.5	83.3	82.9		96.3	97.5	141.3	120.7	108.9	110.0
	96.4	95.4	180.0							
	178.2	178.3								

	pyrophyllite angles									
	O−M−O			M−O−H	M−O−M		Si-O−M		O-Si-O	
	oba-ao-oba	oh-ao-oba	oh-ao-oh	ao-oh-ho	ao-oba-ao	ao-oh-ao	st-ob-st	st-oba-ao	oba-st-ob	ob-st-ob
CLAYFF	82 ± 3	92 ± 5	81 ± 3	119 ± 12	97 ± 3	98 ± 3	144 ± 4	127 ± 4	105 ± 3	113 ± 3
	90 ± 3	169 ± 4					157 ± 4			
	100 ± 4									
	169 ± 4									
AIMD	77 ± 2	94 ± 4	77 ± 2	122 ± 7	102 ± 3	103 ± 3	130 ± 4	126 ± 4	109 ± 3	109 ± 4
	92 ± 3	165 ± 4					144 ± 5			
	99 ± 4									
	164 ± 8									
expt	77.9	95.4	76.5		102.2	103.5	131.6	125.7	109.3	109.9
	92.5	166.1					144.7			
	99.3									
	165.2									

potentials accurately predict the angle distributions of the clay structures. In Table 4, the angles are classified into five general groups, which are O−M−O, M−O−M, Si−O−M, Si−O−Si, and O−Si−O, where M = Al, Mg. Each of these groups is further subdivided on the basis of atom types in the triad. For some angle types (e.g., obss-mgo-obss), several peaks were seen in the distributions. The standard deviation is reported in Table 4 to give an indication of the distribution broadness for each peak.

The talc and pyrophyllite O−M−O angle distributions are shown in Figure 2. Examination of the calculated talc obss-mgo-obss and pyrophyllite oba-ao-oba distributions show remarkable agreement with experiment, where the O−M−O angles near 90° are split into two or three components. Further inspection of the pyrophyllite angle distribution shows a shoulder located near 100°, which is not present in talc. Deconvolution of the shoulder with the PeakFit software[41] gives an additional Gaussian-shaped peak near 100°, in excellent agreement with the experimentally observed angle at 99°. This peak broadening and splitting is due to the dioctahedral sheet stretching normal to the *ab* plane. Furthermore, the pyrophyllite oh-ao-oba angle distribution exhibits a peak near 94° but is split between 85° and 94° in the talc oh-mgo-obss angle distribution. This behavior is indicative of the constrained nature of the trioctahedral system, where no vacancy is present to allow for additional flexibility.

For the O−Si−O, M−O−M, and Si−O−M angles, each of these distributions exhibits a Gaussian-shaped curve centered around the mean (Supporting Information). The major source of discrepancy between the classical CLAYFF model and experiment is noted with the Si−O−Si angles. CLAYFF consistently overpredicts the Si−O−Si angle in both clay materials. The AIMD results are in excellent agreement due to dynamic relaxation of the electronic structure. Given the covalent nature of the Si−O bonds, it is not surprising that a rigid ion model does not capture the observed behavior. Previous classical simulation studies have included 3-body terms for the Si−O−Si angles to capture the SiO_4 tetrahedron structure.[12,19−21] Future modifications to CLAYFF may include 3-body interactions or polarizable models to account for these covalency effects.

The orientation of the hydroxyl group relative to the *ab* plane is compared in Figure 3. The computed hydroxyl orientation angle of talc is centered around 80°, exhibiting a rather narrow distribution. Equivalent results are obtained through AIMD and CLAYFF, where the distribution ranges from 60° to 90°. Given that no vacancies are present in the trioctahedral sheet, the hydroxyl group is forced to point nearly parallel to the *c* axis to minimize the electrostatic repulsion between H and Mg atoms.

The pyrophyllite hydroxyl group behavior is significantly different than talc. The pyrophyllite vacancies have a large influence on hydroxyl orientation, where the distributions are broader and the mean orientation angles are considerably lower. In addition to the structural distinctions between talc and pyrophyllite, there are subtle differences between the ab initio and classical MD simulation results. The average orientation angle relative to the *ab* plane predicted from AIMD simulations is 28 ± 16°, while the mean CLAYFF angle is shifted downward to 15 ± 21°. Furthermore, the CLAYFF distribution exhibits a Gaussian-shaped profile at lower angles but deviates from this behavior with a long tail extending from 30° to 80°. This indicates that there are essentially two prominent hydroxyl orientations, separated by an energetic barrier. The peaks were deconvoluted and shown in Figure 3, giving averages of 5 ± 11° and 32 ± 21°, respectively.

Unfortunately, a direct comparison with experiment cannot be made since the pyrophyllite hydroxyl orientation angles have not been measured. However, there have been hydroxyl orientation angle measurements for the dioctahedral mica, muscovite. Muscovite is a derivative of pyrophyllite, where interlayer cations are present to neutralize the charged layers. Given the structural similarities, the experimentally measured muscovite orientation angle of 16° supports the CLAYFF results for pyrophyllite.[42] In contrast to these results, the AIMD orientation angle results for pyrophyllite are consistent with previous DFT

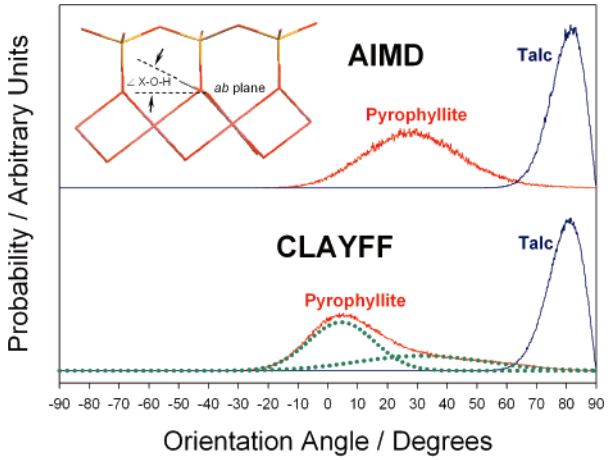

Figure 3. O−H orientation angles relative to the *ab* plane derived from AIMD and CLAYFF are slightly different. The molecular model (inset) illustrates this angle. The solid blue and red are the raw data of talc and pyrophyllite, respectively, while the dotted green lines are the deconvoluted peaks for CLAYFF pyrophyllite.

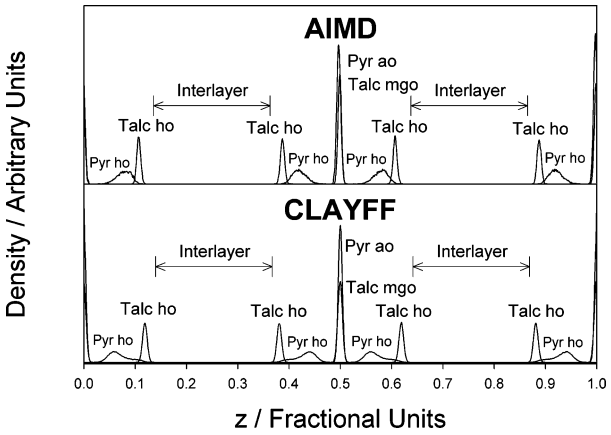

Figure 4. Hydrogen atomic density profiles for pyrophyllite and talc. The ao and mgo atom types are shown for reference. The AIMD results are offset above the CLAYFF results. Note that 1.0 fractional unit ≈ 18 Å.

studies (Bridgeman et al.[5] = 22.2°; Refson et al.[8] = 24.7−26.3°; Sainz-Diaz et al.[9] = 33°; Stackhouse et al.[11] = 26 ± 3°) and electrostatic energy calculations (Giese[43] = 26−31.5°). To resolve these issues, additional simulations of muscovite were conducted. The AIMD orientation angle of 15 ± 17° is in excellent agreement with previous experiments, while CLAYFF predicted a slightly negative orientation angle of −3 ± 14°.

However, as noted above, deconvolution of the angle distribution for the CLAYFF simulation suggests two local orientations for the hydroxyl in pyrophyllite. The broad smaller peak at 32° most likely is an artifact associated with the atom-centered nature of CLAYFF, whereas the DFT model utilizes the distribution of electrons (and electrostatic potential) about the siloxane cavity and affects the hydroxyl position.

Figure 4 shows the hydrogen atomic density profiles along the *z* axis for two layers of talc and pyrophyllite, respectively. The octahedral metals are also shown for reference. The agreement between AIMD and CLAYFF for the talc atomic density is outstanding, where the hydrogen is located nearly 0.1 fractional unit (1.8 Å) away from the octahedral sheet center. Examination of the hydrogen locations in pyrophyllite shows a distinctive shift toward the octahedral sheet, indicative of smaller orientation angles. Furthermore, the shift is much broader and more pronounced for CLAYFF than AIMD. The CLAYFF results also have a significant tail extending away from the octahedral sheet, consistent with the orientation angle distribution results in Figure 3.

Power Spectra. For vibrational frequencies, we chose to use power spectra analysis, which includes thermal effects at the simulated temperature. An additional advantage of power spectra is that contributions from individual atom types can be probed. However, spectral peaks cannot be assigned to normal modes and must be inferred by examining the atom types involved. Power spectra of individual atom types are shown in Figure 5. In addition to the issues related to the assignment of peaks, large system sizes and long simulation time scales are required for smooth power spectra.[44] For the AIMD results, there is a significant amount of noise in the power spectra, making peak assignments especially difficult. In these cases, we have applied the Savitzky-Golay smoothing techniques available within the PeakFit software.[41] As a result, the AIMD peak assignments are conservative at best, where only the prominent peaks are included in the analysis. This clearly illustrates the need to develop better force fields for classical simulations in order to obtain reliable statistics.

To further assist in peak assignments, normal-mode analysis calculations were conducted using DFT and CLAYFF (Materials Studio Discover and DMOL[3] modules[40]). In a normal-mode analysis, the symmetry and atomic contribution to each mode can be obtained, but the calculation is based on a geometry optimized structure corresponding to a temperature of 0 K. Animations of selected normal modes are given as Supporting Information. It is important to note that animations of the normal modes indicate that most of the vibrational modes are actually a combination of bond stretches with lattice vibrations (bends, twists, etc.).

Vibrational frequencies as calculated from the Fourier-transformed VACF are given in Table 5. We focus our analysis on two regions of importance to experimental spectra: the O−H stretching mode (3650−3750 cm^{-1}) and the Si−O stretching modes (900−1200 cm^{-1}). Vibrational frequencies of pyrophyllite and talc are reviewed by Farmer.[45] The frequencies are also compared with recent FT Raman spectra of montmorillonite, particularly for the SiO_4 tetrahedral modes around 700 cm^{-1}. Previous computational frequencies listed in Table 5 come from a DFT normal-mode analysis of pyrophyllite[9] and an MD simulation of talc using a completely bonded force field.[46]

For both clays, the O−H bond stretch frequencies obtained from the AIMD power spectra are within 20 cm^{-1} of the experimental values. For CLAYFF, the O−H frequencies are approximately 75 cm^{-1} higher than experiment. The CLAYFF O−H stretch frequency depends primarily on the O−H bond stretch term in the force field.[22] Adjustments to the harmonic spring constant and equilibrium bond length may be necessary to match the vibrational spectra. The other prominent modes featured in spectroscopic studies of clays are three Si−O stretching modes, which typically occur between 900 and 1200 cm^{-1} and are shown in Figure 6. These modes occur at higher frequencies in pyrophyllite than in talc, in agreement with experiment through AIMD and CLAYFF.[45]

For pyrophyllite, we used the atomic power spectra and normal-mode analyses to identify Si−O stretch modes, O−H librational modes, and tetrahedral SiO_4 bend modes seen in Raman spectra. In general, the simulated Si−O stretching frequencies between 1000 cm^{-1} and 1210 cm^{-1} agree with experiment. Recent polarized attenuated total reflectance FTIR spectra of two charged smectites indicate four Si−O frequencies in this region, but the peak at 1086 cm^{-1} is influenced by the

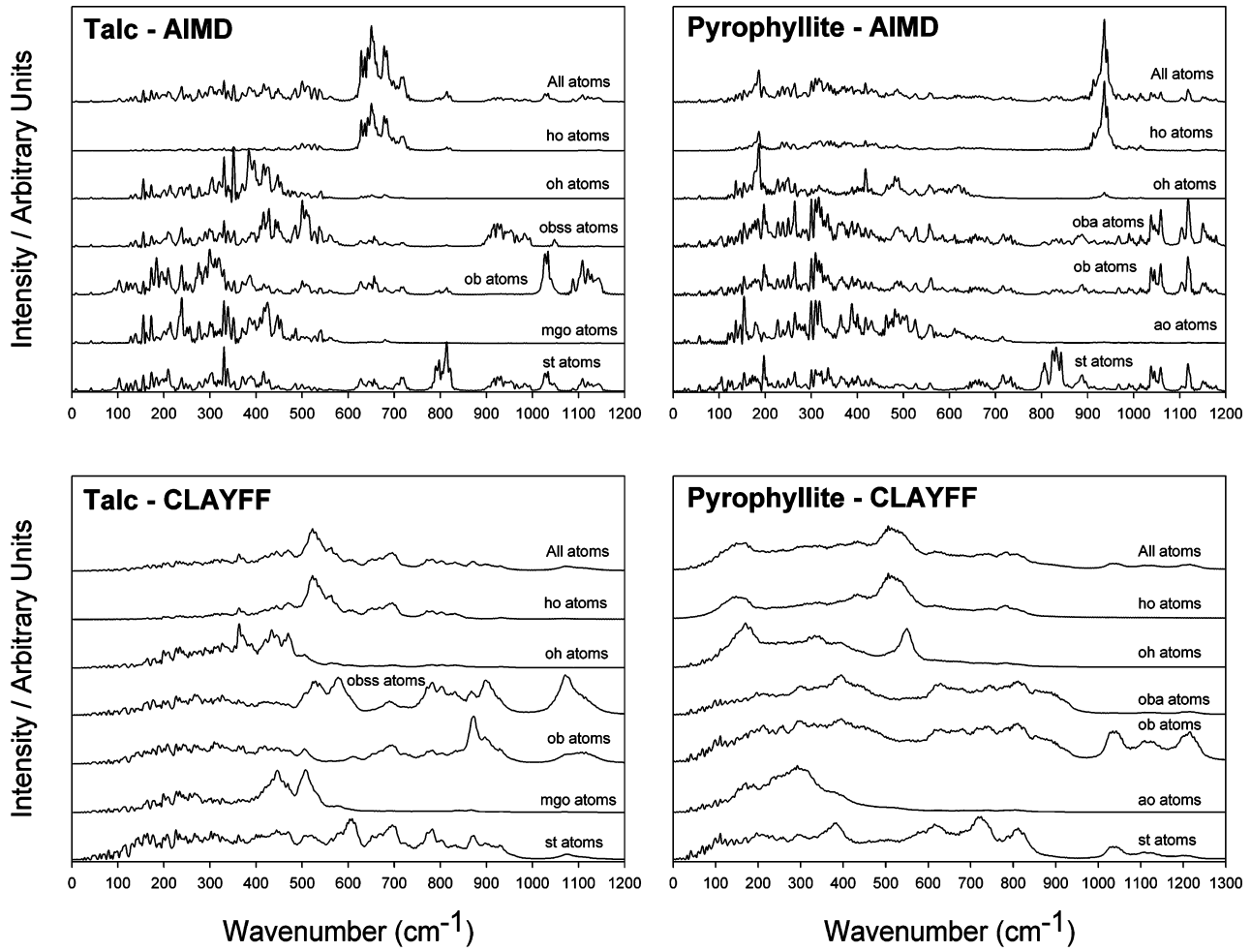

Figure 5. AIMD and CLAYFF power spectra of pyrophyllite and talc. The individual atomic contributions are offset from one another.

TABLE 5: Vibrational Frequencies (cm^{-1}) from Power Spectra Calculations

clay	mode	CLAYFF (this work)	AIMD (this work)	computational literature[a,b]	experimental[c]
pyrophyllite	O−H stretch	3750	3658	3655	3675
	Si−O stretch	1210, 1120, 1035	1160, 1115, 1050, 1000	1073−973	1121, 1070, 1050
	O−H libration	790	935	951, 948, 921	915−950
	Raman SiO_4 bend (a_1)	810, 730, 625	885, 835, 730		708[d]
	O−H libration + lattice breathing	165	185		≈200
talc	O−H stretch	3750	3669	3854−3880	3677
	Si−O stretch	1075, 935	1120, 1035, 930	1075, 921, 737	1039, 1014, 890
	Si−O bend/O−H libration	785, 695, 610, 525	815, 715, 675, 650, 510	435, 310, 278	687, 669, 535, 465, 450
	Mg vibration	445	245, 205	227	197, 177

[a] Pyrophyllite results (DFT): Sainz-Diaz et al.[9] [b] Talc results (MD): Arab et al.[46] [c] Experimental IR results: V. C. Farmer.[45] [d] Raman results of Na-montmorillonite: Frost and Rintoul.[48]

presence of an electrical double layer at the siloxane surface.[47] The influence of interlayer water and ions on Si−O stretching modes will be the subject of future work. The strong O−H libration mode is observed at 935 cm^{-1} in the AIMD spectrum and is a signature mode of the octahedral vacancies in pyrophyllite. However, the CLAYFF force field underpredicts this frequency at 790 cm^{-1}. This is an indication that modifications to the hydroxyl group interactions within CLAYFF are necessary for an adequate description of the vibrational modes and sorptive nature of the clay minerals. Additional Si−O modes are seen between 625 cm^{-1} and 885 cm^{-1}, which are attributed to SiO_4 tetrahedra. These modes are prominent in the Raman spectrum of montmorillonite.[48] We notice that these Si−O modes are accompanied by lattice modes involving AlO_6 octahedra and O−H librations. The prominent peak in the near-IR region (165 cm^{-1} and 185 cm^{-1} for CLAYFF and AIMD, respectively) is a combination of O−H libration and lattice breathing.

For talc, the contribution of siloxane O atoms (ob atom type) and apical O atoms (obss atom type) differs among the Si−O stretch modes. The CLAYFF peak at 1075 cm^{-1} mainly involves Si and the obss atom type. This peak has a broad shoulder, indicating a minor peak near 1115 cm^{-1} with equal intensity for ob and obss atom types. The AIMD atomic spectra indicate that the modes at 1120 cm^{-1} and 930 cm^{-1} involve mainly Si with the ob and obss atom types, respectively. The mode at

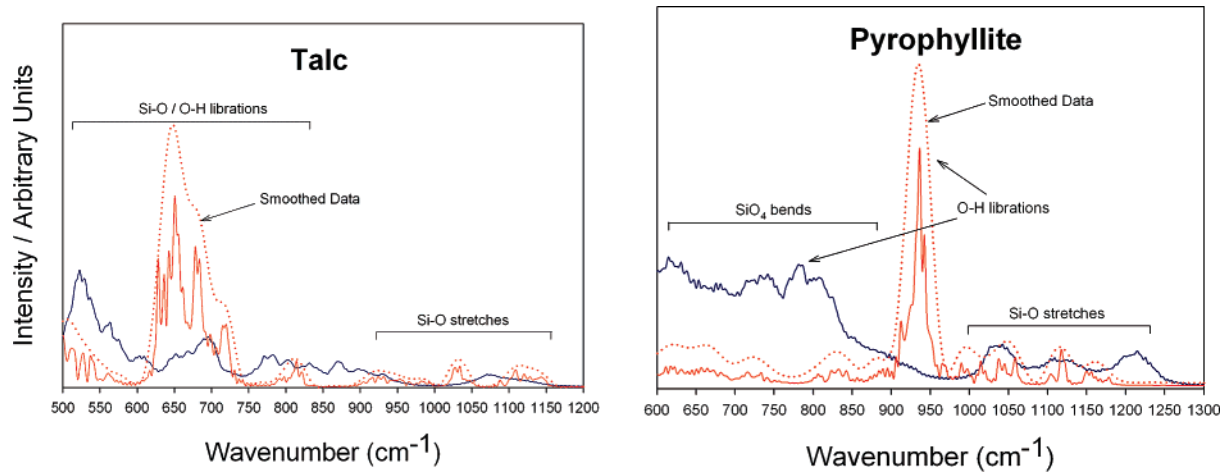

Figure 6. CLAYFF (blue) and AIMD (red) power spectra for talc and pyrophyllite. The smoothed data are given with the dotted lines.

1035 cm^{-1} is due to the ob atom type, with a shoulder at 1050 cm^{-1} due to the obss atom type. The high-frequency O−H libration mode (935 cm^{-1}) is absent because there are no octahedral vacancies in talc. The talc Si−O bend and O−H libration modes between 510 cm^{-1} and 815 cm^{-1} are listed together in Table 5 because of the extensive coupling of these modes (Figure 5). For CLAYFF, atomic spectra indicate that Si, O, and H atoms participate in each mode in this region. For AIMD, the modes at 510 cm^{-1} and 675 cm^{-1} involve primarily O−H librations.

Conclusions

In general, the hydroxyl group structure is difficult to characterize through experiment but essential to a fundamental understanding of clay interfacial and adsorption behavior. Atomistic simulations provide an alternative perspective with which to understand the experiments and to provide a molecular-scale picture of the hydroxyl interactions. CLAYFF yields a reasonably accurate description of the bulk structural properties of clay minerals. However, from the structural and vibrational analysis presented here, we identify four areas in which CLAYFF results differ from AIMD and experiment: (1) O−H bond length, (2) Si−O−Si angle distribution, (3) O−H orientation angle with respect to the *ab* plane, and (4) Al_2OH vibration. For each clay, the CLAYFF O−H bond length is consistently found to be 0.06 Å longer than the average AIMD O−H bond length. Although the AIMD bond length is consistent with previous DFT calculations,[4,6,8,9,11] no reliable experimental data on the O−H bond length exists. In understanding the interplay between the molecular structure and vibrational spectroscopy, additional modifications to CLAYFF will be necessary to adequately model the structural, vibrational, and adsorption properties of clay minerals.

Acknowledgment. We acknowledge support from the U.S. Department of Energy, Office of Basic Energy Sciences, Geosciences Research. Sandia is a multiprogram laboratory operated by Sandia Corporation, a Lockheed Martin company, for the U.S. Department of Energy under Contract No. DE-AC04-94AL85000.

Supporting Information Available: Additional angle distributions and animations of the vibrational modes. This material is available free of charge via the Internet at http://pubs.acs.org.

References and Notes

(1) Bailey, S. W. *Rev. Mineral.* **1988**, *19*, 1.
(2) Brindley, G. W.; Brown, G. *Crystal Structures of Clay Minerals and their X-ray Identification*; Mineralogical Society: London, 1980.
(3) Kubicki, J. D.; Bleam, W. F. *Molecular Modeling of Clays and Mineral Surfaces*; The Clay Minerals Society: Aurora, Colorado, 2003; Vol. 12.
(4) Bickmore, B. R.; Rosso, K. M.; Nagy, K. L.; Cygan, R. T.; Tadanier, C. J. *Clays Clay Miner.* **2003**, *51*, 359.
(5) Bridgeman, C. H.; Buckingham, A. D.; Skipper, N. T.; Payne, M. C. *Mol. Phys.* **1996**, *89*, 879.
(6) Chatterjee, A.; Iwasaki, T.; Ebina, T. *J. Phys. Chem. A* **2000**, *104*, 8216.
(7) Churakov, S. V. *J. Phys. Chem. B* **2006**, *110*, 4135.
(8) Refson, K.; Park, S. H.; Sposito, G. *J. Phys. Chem. B* **2003**, *107*, 13376.
(9) Sainz-Diaz, C. I.; Escamilla-Roa, E.; Hernandez-Laguna, A. *Am. Mineral.* **2004**, *89*, 1092.
(10) Sainz-Diaz, C. I.; Timon, V.; Botella, V.; Artacho, E.; Hernandez-Laguna, A. *Am. Mineral.* **2002**, *87*, 958.
(11) Stackhouse, S.; Coveney, P. V.; Sandre, E. *J. Am. Chem. Soc.* **2001**, *123*, 11764.
(12) Teppen, B. J.; Yu, C. H.; Newton, S. Q.; Miller, D. M.; Schafer, L. *J. Phys. Chem. A* **2002**, *106*, 5498.
(13) Scholtzova, E.; Tunega, D.; Nagy, L. T. *J. Mol. Struct.* **2003**, *620*, 1.
(14) Balan, E.; Saitta, A. M.; Mauri, F.; Calas, G. *Am. Mineral.* **2001**, *86*, 1321.
(15) Benco, L.; Tunega, D.; Hafner, J.; Lischka, H. *J. Phys. Chem. B* **2001**, *105*, 10812.
(16) Benco, L.; Tunega, D.; Hafner, J.; Lischka, H. *Am. Mineral.* **2001**, *86*, 1057.
(17) Tosoni, S.; Doll, K.; Ugliengo, P. *Chem. Mater.* **2006**, *18*, 2135.
(18) Tunega, D.; Gerzabek, M. H.; Lischka, H. *J. Phys. Chem. B* **2004**, *108*, 5930.
(19) Bougeard, D.; Smirnov, K. S.; Geidel, E. *J. Phys. Chem. B* **2000**, *104*, 9210.
(20) Heinz, H.; Koerner, H.; Anderson, K. L.; Vaia, R. A.; Farmer, B. L. *Chem. Mater.* **2005**, *17*, 5658.
(21) Teppen, B. J.; Rasmussen, K.; Bertsch, P. M.; Miller, D. M.; Schafer, L. *J. Phys. Chem. B* **1997**, *101*, 1579.
(22) Cygan, R. T.; Liang, J.-J.; Kalinichev, A. G. *J. Phys. Chem. B* **2004**, *108*, 1255.
(23) Braterman, P. S.; Cygan, R. T. *Am. Mineral.* **2006**, *91*, 1188.
(24) Kalra, A.; Parks, D. M.; Rutledge, G. C. *Macromolecules* **2007**, *40*, 140.
(25) Greathouse, J. A.; Cygan, R. T. *Phys. Chem. Chem. Phys.* **2005**, *7*, 3580.
(26) Greathouse, J. A.; Cygan, R. T. *Environ. Sci. Technol.* **2006**, *40*, 3865.
(27) Wang, J. W.; Kalinichev, A. G.; Kirkpatrick, R. J. *Geochim. Cosmochim. Acta* **2006**, *70*, 562.
(28) Perdikatsis, B.; Burzlaff, H. *Z. Kristallografiya* **1981**, *156*, 177.
(29) Lee, J. H.; Guggenheim, S. *Am. Mineral.* **1981**, *66*, 350.
(30) Kresse, G.; Furthmuller, J. *Phys. Rev. B* **1996**, *54*, 11169.
(31) Kresse, G.; Furthmuller, J. *Comput. Mater. Sci.* **1996**, *6*, 15.
(32) Blochl, P. E. *Phys. Rev. B* **1994**, *50*, 17953.

(33) Kresse, G.; Joubert, D. *Phys. Rev. B* **1999**, *59*, 1758.
(34) Perdew, J. P.; Wang, Y. *Phys. Rev. B* **1992**, *45*, 13244.
(35) Asthagiri, D.; Pratt, L. R.; Kress, J. D. *Phys. Rev. E* **2003**, *68*.
(36) Allen, M. P.; Tildesley, D. J. *Computer Simulation of Liquids*; Clarendon Press: Oxford, 1987.
(37) Plimpton, S. J.; Pollock, R.; Stevens, M. *Particle-Mesh Ewald and rRESPA for parallel molecular dynamics simulation*s; Eighth SIAM Conference on Parallel Processing for Scientific Computing, 1997.
(38) Ponder, J. W. TINKER: Software Tools for Molecular Design,-version 4.2; June 2004.
(39) Press, W. H.; Teukolsky, S. A.; Vetterling, W. T.; Flannery, B. P. *Numerical Recipes : The Art of Scientific Computing*; Cambridge University Press: Cambridge, 1986.
(40) *Accelrys*. Materials Studio Release Notes, release 4.1; Accelrys Software, Inc.: San Diego, CA, 2006.
(41) *SeaSolve*. PeakFit: Peak Separation and Analysis Software, version 4; 2003.
(42) Beran, A. Infrared spectroscopy of micas. In *Micas: Crystal Chemistry and Metamorphic Petrology*, vol. 46; 2002; p 351.
(43) Giese, R. F. *Clays Clay Miner.* **1979**, *27*, 213.
(44) Kleinhesselink, D.; Wolfsberg, M. *Surf. Sci.* **1992**, *262*, 189.
(45) Farmer, V. C. The Layer Silicates. In *The Infrared Spectra of Minerals*; Farmer, V. C., Ed.; Mineralogical Society: London, 1974; p 331.
(46) Arab, M.; Bougeard, D.; Smirnov, K. S. *Phys. Chem. Chem. Phys.* **2002**, *4*, 1957.
(47) Johnston, C. T.; Premachandra, G. S. *Langmuir* **2001**, *17*, 3712.
(48) Frost, R. L.; Rintoul, L. *Appl. Clay Sci.* **1996**, *11*, 171.